

A Solar Source of Alfvénic Magnetic Field Switchbacks: In Situ Remnants of Magnetic Funnels on Supergranulation Scales

```
S. D. Bale<sup>1,2</sup>, T. S. Horbury<sup>3</sup>, M. Velli<sup>4</sup>, M. I. Desai<sup>5,6</sup>, J. S. Halekas<sup>7</sup>, M. D. McManus<sup>1,2</sup>, O. Panasenco<sup>8</sup>, S. T. Badman<sup>1,2</sup>, T. A. Bowen<sup>2</sup>, B. D. G. Chandran<sup>9,10</sup>, J. F. Drake<sup>11,12,13</sup>, J. C. Kasper<sup>14,15</sup>, R. Laker<sup>3</sup>, A. Mallet<sup>2</sup>, L. Matteini<sup>3</sup>, T. D. Phan<sup>2</sup>, N. E. Raouafi<sup>16</sup>, J. Squire<sup>17</sup>, L. D. Woodham<sup>3</sup>, and T. Woolley<sup>3</sup>, and T. Woolley<sup>3</sup>, T. D. Physics Department, University of California, Berkeley, CA 94720-7300, USA; bale@berkeley.edu

Space Sciences Laboratory, University of California, Berkeley, CA 94720-7450, USA

The Blackett Laboratory, University of California, Berkeley, CA 94720-7450, USA

Southwest Research Institute, 6220 Culebra Road, San Antonio, TX 78238, USA

University of Texas at San Antonio, San Antonio, TX 78249, USA

Department of Physics and Astronomy, University of Iowa, Iowa City, IA 52242, USA

Advanced Heliophysics, Pasadena, CA 91106, USA

Department of Physics & Astronomy, University of New Hampshire, Durham, NH 03824, USA

Department of Physics, University of New Hampshire, Durham, NH 03824, USA

Institute for Physical Science and Technology, University of Maryland, College Park, MD 20742, USA

Isolint Space Science Institute, University of Maryland, College Park, MD 20742, USA

BWX Technologies, Inc., Washington DC 20002, USA

Science Institute, University of Michigan, Ann Arbor, MI 48109, USA

The Johns Hopkins Applied Physics Laboratory, Laurel, MD 20723, USA

The Johns Hopkins Applied Physics Laboratory, Laurel, MD 20723, USA

Physics Department, University of Otago, Dunedin 9010, New Zealand

Received 2021 September 1; revised 2021 October 5; accepted 2021 October 5; published 2021 December 20
```

Abstract

One of the striking observations from the Parker Solar Probe (PSP) spacecraft is the prevalence in the inner heliosphere of large amplitude, Alfvénic magnetic field reversals termed *switchbacks*. These $\delta B_R/B \sim \mathcal{O}(1)$ fluctuations occur over a range of timescales and in *patches* separated by intervals of quiet, radial magnetic field. We use measurements from PSP to demonstrate that patches of switchbacks are localized within the extensions of plasma structures originating at the base of the corona. These structures are characterized by an increase in alpha particle abundance, Mach number, plasma β and pressure, and by depletions in the magnetic field magnitude and electron temperature. These intervals are in pressure balance, implying stationary spatial structure, and the field depressions are consistent with overexpanded flux tubes. The structures are asymmetric in Carrington longitude with a steeper leading edge and a small (\sim 1°) edge of hotter plasma and enhanced magnetic field fluctuations. Some structures contain suprathermal ions to \sim 85 keV that we argue are the energetic tail of the solar wind alpha population. The structures are separated in longitude by angular scales associated with supergranulation. This suggests that these switchbacks originate near the leading edge of the diverging magnetic field funnels associated with the network magnetic field—the primary wind sources. We propose an origin of the magnetic field switchbacks, hot plasma and suprathermals, alpha particles in interchange reconnection events just above the solar transition region and our measurements represent the extended regions of a turbulent outflow exhaust.

Unified Astronomy Thesaurus concepts: Solar wind (1534)

1. Introduction

The NASA Parker Solar Probe (PSP) mission (Fox et al. 2016) was executed to make direct in situ measurements of the source regions of the solar wind and to understand the heating and acceleration mechanisms using those measurements. A foundational observation from PSP has been the prevalence of large $\delta B_R/B \sim \mathcal{O}(1)$ Alfvénic field reversals that had earlier been termed switchbacks (hereafter SBs), which are interspersed among intervals of quiet primarily radial magnetic field (Bale et al. 2019; Kasper et al. 2019; Dudok de Wit et al. 2020; Horbury et al. 2020). While SBs have been identified previously using spacecraft measurements at 0.3 au (Horbury et al. 2018), at 1 au (Gosling et al. 2009, 2011) and at high solar latitudes (Balogh et al. 1999; Matteini et al. 2014), the PSP measurements are notable for the abundance of events and the apparent patterns of SBs and quiet wind. Several models of SB generation and evolution have been developed recently with sources in velocity shear in the corona (Landi et al. 2005; Ruffolo et al. 2020;

Schwadron & McComas 2021), magnetic reconnection (Fisk & Kasper 2020; Zank et al. 2020; Drake et al. 2021), impulsive energy injection within magnetic funnels (Magyar et al. 2021a, 2021b), and the nonlinear radial evolution of large-amplitude Alfvénic fluctuations (Landi et al. 2006; Squire et al. 2020; Mallet et al. 2021; Shoda et al. 2021). A key question is whether the SBs are generated at the source of the solar wind, and serve as a fundamental diagnostic of the energization mechanism, or if rather they are a product of radial evolution.

Because of their ubiquity, and apparent nonlinearity, the possibility that SBs provide a direct, in situ diagnostic of solar wind heating or energization is tantalizing. A variety of heating mechanisms have been proposed: nanoflares, wave dissipation, footpoint shearing, magnetic reconnection, and turbulence, to name a few. Most of these theories find some support in remote sensing or in situ data and many of them rely in impulsive magnetic activity at the coronal base. There are many good review papers on the topic, including recently by Cranmer & Winebarger (2019).

Here, we use PSP measurements to demonstrate that an interval of periodically modulated SBs observed below 25 solar radii (R_S) of PSP Encounter 06 is related directly to underlying photospheric magnetic field concentrations. While the bulk radial proton (solar wind) speed here ranges from 200–400 km s⁻¹, these measurements are akin to the *microstream* structures measured previously in the fast solar wind (Neugebauer et al. 1995). However, these intervals are clearly pressure balanced, hence spatially stable, and show enhanced alpha particle abundance, hot proton beams, energetic particles, and depressed electron temperature—all suggestive of fast wind-like sources. The alpha particles are heated to $T_{\alpha} \geqslant 8T_{p}$ and the temperature anisotropies of the alpha particles and beam protons suggest a common origin and/or evolution. The ballistically mapped longitudinal source structure and the presence of suprathermal ions suggests a source at the edge of magnetic funnels associated with interchange reconnection. A narrow (\sim 1°) leading edge shows enhanced proton parallel heating, similar to measurements from Helios at the leading edge of high speed streams (Marsch et al. 1982).

We present a schematic scenario of the source suggesting that PSP is transiting through the coronal extension of magnetic funnels (Kopp & Kuperus 1968; Gabriel 1976; Dowdy et al. 1986; Tu et al. 2005) and possibly plumes (Wilhelm et al. 2011; Poletto 2015) associated with the photospheric network magnetic field, where the Alfvénic SBs are generated. The underlying magnetic configuration should be favorable to interchange magnetic reconnection between adjacent funnels and/or closed loop structure above the photosphere, as developed in the furnace solar wind model of Axford et al. (1999). Reconnection would also explain the energetic ions and the inherent intermittent nature of the SBs. Although we highlight the impact of processes and structure in the low solar atmosphere, some properties of SBs may develop or be further amplified by in situ evolution in the solar wind, which increases $\delta B_R/B_0$ and can lead to abrupt rotations of B (e.g., Squire et al. 2020; Mallet et al. 2021; Shoda et al. 2021).

2. PSP Measurements and Context

We use magnetic field and electron density measurements from the FIELDS instrument (Bale et al. 2016), plasma ion and electron measurements from the Solar Wind Electrons Alphas and Protons (SWEAP) instrument suite (Kasper et al. 2016), and energetic ion measurements from the Integrated Science Investigation of the Sun (ISOIS) suite (McComas et al. 2016) on the NASA PSP spacecraft (Fox et al. 2016). Measurements are made near perihelion of PSP Encounter 06 from 2020 September 27-28 when the spacecraft was between 20.4-22.7 solar radii (R_S) from the Sun center and $232^{\circ}-270^{\circ}$ heliographic (HG) longitude; the spacecraft trajectory dips south of the ecliptic near perihelion and was below -3° HG latitude during this interval and stayed below the heliospheric current sheet (HCS). Perihelion at 20.39 R_S occurred at 09:16 UT on 2020 September 27. The spacecraft tangential (Keplerian) speed in HG coordinates ranges from 87 km s⁻¹ at the start of the interval to 68 km s⁻¹ at the end, passing through the maximum $89 \,\mathrm{km \, s^{-1}}$ at perihelion. The spacecraft radial speed ranges from -11 km s^{-1} at the start of the interval to 39 km s^{-1} at the end, passing through the 0 km s^{-1} at perihelion. The measurements we analyze here are primarily in the outbound leg of the orbit.

Figure 1 shows the magnetic connectivity of the PSP spacecraft footpoints from the source surface (SS) at $R_{\rm SS} = 2.2~R_{\rm S}$ mapped down the solar surface, near the low latitude boundary of a coronal hole (CH) feature at -60° HG latitude. The mapping uses



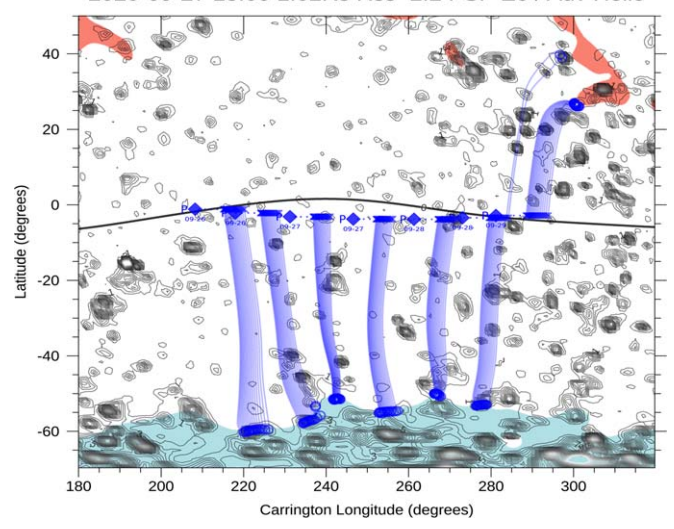


Figure 1. Magnetic field connectivity during PSP Encounter 06. The perihelion loop is seen between 210° and 300° Carrington (HG) longitude. A PFSS model (described in the text) maps PSP magnetic connection (in 12 hr intervals) from the SS at 2.2 Rs to the height 1.02 Rs above the photosphere. A solid black line shows the model neutral line on the source surface. Black contours indicate magnetic field pressure at 1.02 Rs (\sim 14 Mm) showing the spatial scales associated with network magnetic field and supergranulation cell boundaries. During the interval studied here, the SS was connected to the southern CH boundary near -60° Carrington latitude. The ballistic projection of the PSP trajectory (blue diamonds) on the SS (blue crosses) and down to the solar wind source regions (blue circles) calculated for the height R = 1.02 R_S and measured in situ solar wind speed \pm 80 km s $^{-1}$. Open magnetic field regions are shown in blue (negative) and pink (positive). The B^2 map is calculated for 2020 September 27, different PSP positions along the trajectory shown for selected days are displayed under the blue diamonds with a time cadence of 12 hr during 2020 September 26–29.

a Potential Field Source Surface (PFSS) model (Altschuler & Newkirk 1969; Schatten et al. 1969; Hoeksema 1984) as implemented by Schrijver & De Rosa (2003). PFSS has proved to be remarkably robust during early PSP (solar minimum) orbits (Bale et al. 2019; Badman et al. 2020; Panasenco et al. 2020). As a lower boundary condition, the PFSS model incorporates magnetic field maps produced by an evolving surface-flux transport model based on magnetic fields observed by the Helioseismic and Magnetic Imager (Scherrer et al. 2012; Schou et al. 2012) on the Solar Dynamics Observatory. The model evolves these fields in accordance with empirical prescriptions for differential rotation, meridional flows, and convective dispersal processes. PFSS models are parameterized by a radial distance at which all magnetic field lines become open and radial: the SS height. This is typically set at $R_{SS} = 2.5 R_S$, but is a free parameter of the model and we choose $R_{SS} = 2.2 R_S$ to be compatible with in situ magnetic field measurements by PSP and Solar Orbiter for this time interval (Telloni et al. 2021).

Black contours in Figure 1 indicate magnetic field pressure at $1.02~R_S~(\sim 14~{\rm Mm}$ altitude above the photosphere) and reveal a network of stronger magnetic field concentrations, which can be inferred up to $\sim 1.04~R_S$, or $28-30~{\rm Mm}$ and then quickly dissipate higher in the corona due to magnetic field line expansion. This low altitude, about 10 times the height of the chromosphere, is found to be critical in filament channel formation and dynamics (Panasenco & Velli 2009) and is comparable to a typical supergranulation cell diameter. The boundary of the southern CH along which PSP footpoints were moving has a sequence of these magnetic concentrations (nodes) with much weaker field between; we estimate from PFSS that PSP crossed 6–8 strong

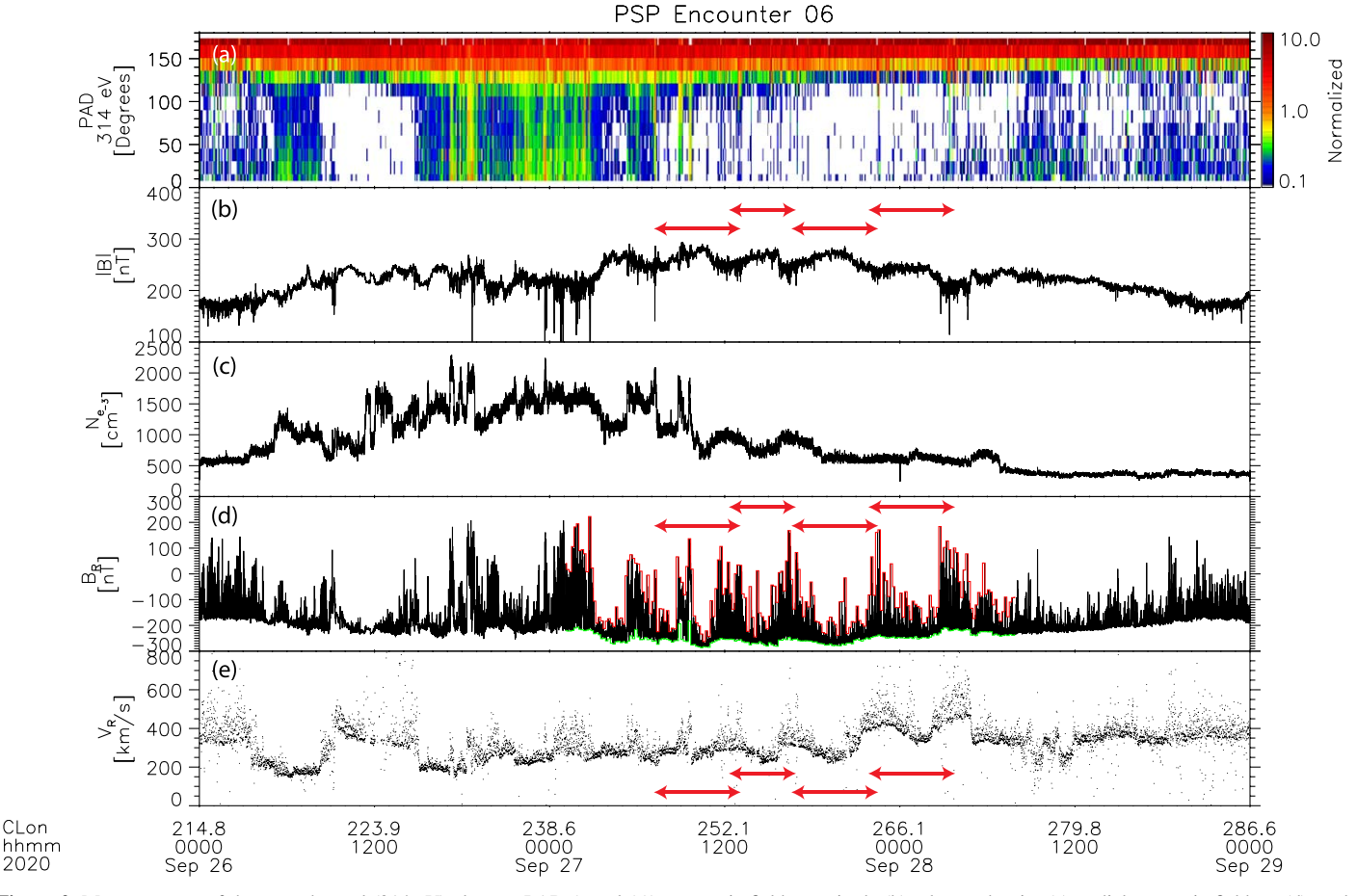


Figure 2. Measurements of the suprathermal (314 eV) electron PAD (panel (a)), magnetic field magnitude (b), plasma density (c), radial magnetic field B_R (d), and radial proton core velocity V_R (e) during the PSP Encounter 06 perihelion. Red horizontal arrows highlight the magnetic field compressions/depletions, velocity modulations, and the accompanying modulations in the SB occurrence and amplitude. The red and green bars in panel (d) are the 10 minute minimum and maximum values of B_R . The ballistically mapped Carrington longitude is shown at the bottom: these modulations occur on angular scales of a few degrees. The outward electron strahl flux implies that the field geometry is uniform outward.

field concentrations during the September 26–29 interval studied here. Note that this PSP perihelion occurred behind the limb, so that there were no current magnetogram data available for the longitudes below the spacecraft. Hence, there is no expectation of a one-to-one correspondence between individual network field concentrations seen in the PFSS, which evolve on timescales of several hours (Rieutord & Rincon 2010), and our in situ measurements.

Proton beam and core parameters are obtained by fitting drifting bi-Maxwellians to the SWEAP/SPAN-Ion proton spectra. The proton beam is constrained to lie along the magnetic field direction relative to the core velocity. For the alpha parameters, four successive spectra were first summed together to obtain better statistics. The SPAN-Ion alpha channel contains a small ($\sim 2\%$) proton contamination. This is compensated for by taking the previously fitted proton parameters and scaling the total density to represent the spurious protons in the alpha channel. This scaled down function, as well as a single bi-Maxwellian to represent the alpha particles, are then fitted to the alpha channel counts spectra and the alpha core parameters obtained. The exact scaling factor from proton channel to alpha channel is a free parameter in the fit, and it was confirmed that there was no energy or angle dependence to the proton contamination, so that an overall simple scaling was sufficient. Distribution functions are fitted only when the solar wind distribution is within the SPAN-Ion field of view (e.g., Woodham et al. 2021). For a more detailed discussion of

SPAN-Ion fitting procedures, see (Finley et al. 2021). SWEAP/SPAN-E measurements (Kasper et al. 2016; Whittlesey et al. 2020) are used to determine electron core and strahl parameters by a combination of fitting and partial moment calculations, as described in Halekas et al. (2020). The electron core component is fitted to a drifting bi-Maxwellian function and the halo component, where present at measurable levels, to an isotropic non-drifting Maxwellian function. Partial moments of the strahl are computed by integrating over the residual of the measured distribution with respect to the core (and halo, if present), for the portion of the distribution in the strahl direction, within 45° of the magnetic field, and for velocities greater than two thermal speeds.

Magnetic field and plasma measurements from PSP Encounter 06 are shown in Figure 2. A normalized (to 90°) pitch angle distribution (PAD) of 314 eV suprathermal (strahl) electrons after \sim 01:00 on 2020 September 27 show primarily outward flux along $-B_R$ indicating a unipolar magnetic field geometry below and consistent with the PSP trajectory being below the HCS as implied in Figure 1. Periodic modulations of the magnetic field magnitude |B| (panel (b)) and radial proton core velocity V_R (panel (e)) are emphasized using red arrows. Panel (d) shows the radial component of the magnetic field B_R and the minimum (green) and maximum (red) value envelopes in 10 minute intervals. The B_R dynamics are dominated by magnetic field SBs (Bale et al. 2019; Horbury et al. 2020) that here are clearly modulated in occurrence and amplitude by the structure in |B| and V_R . Small plasma density

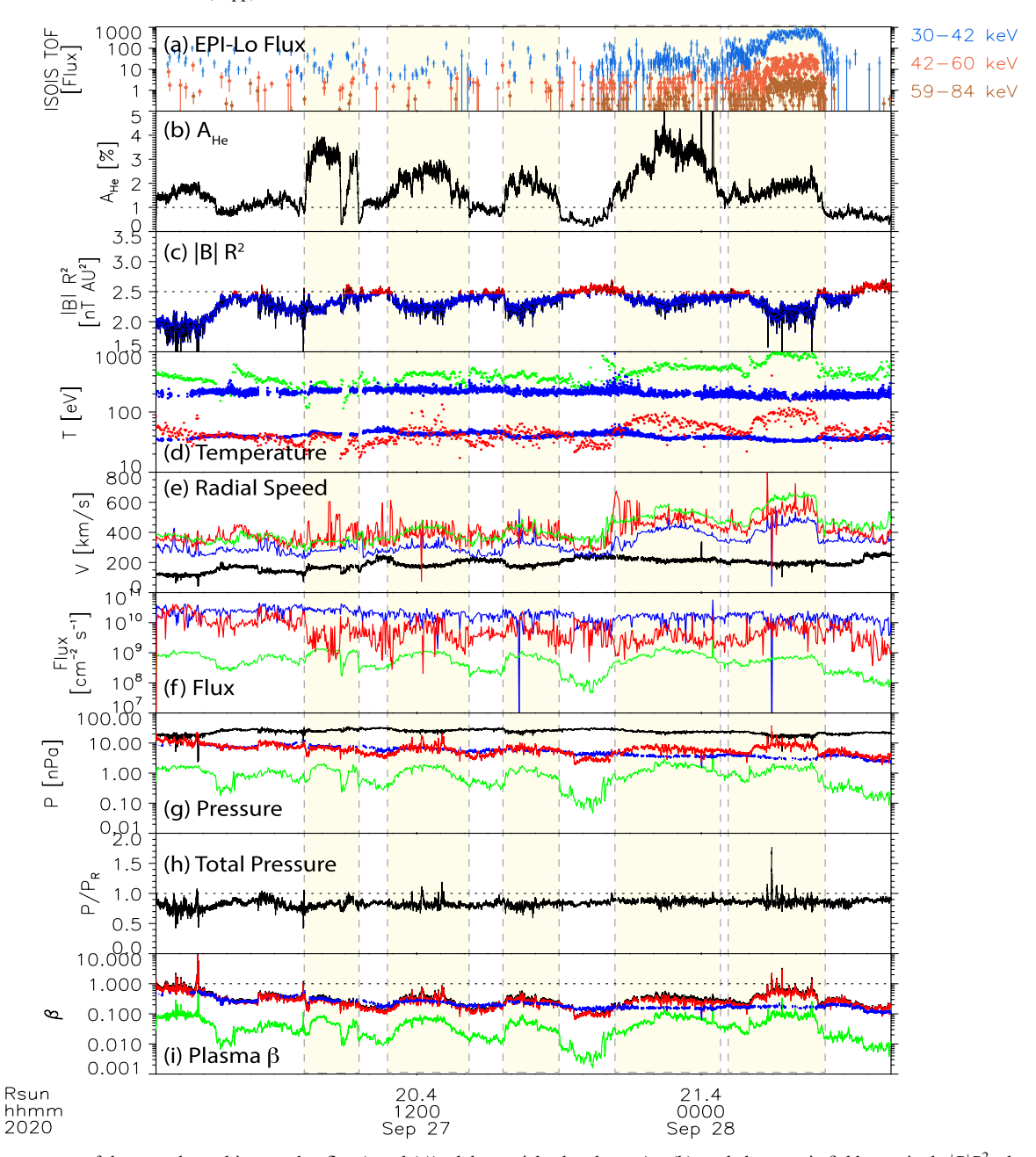


Figure 3. Measurements of the suprathermal ion number flux (panel (a)), alpha particle abundance $A_{\rm He}$ (b), scaled magnetic field magnitude $|B|R^2$, electron core and strahl temperatures (blue), core proton temperature (red), and alpha temperature (green) in panel (d), radial velocities (core proton = blue, alpha = green, proton beam = red) and Alfvén speed (black) in panel (e). Number flux of core protons (blue), alphas (green) and beam protons (red) is in panel (f) and plasma pressures (core proton = red, alpha = green, electron = blue) and magnetic field energy density (black) in panel (g). Panel (h) is the total pressure, plasma, and magnetic, scaled by its fitted radial scaling $p \propto r^{-3.17}$. The bottom panel shows plasma beta (red = core proton, green = alpha, blue = core electron). The intervals of depressed field (panel (b)), which correspond to enhanced SBs, have enhancements in alpha abundance $A_{\rm He}$ consistent with fast solar wind values. Likewise, the intervals of enhanced SBs have higher speed radial wind speeds (panel (d)) with (core) Mach ~1 near the edges but higher Mach flows in the center. Ion temperatures are higher within these structures and electron temperatures are slightly lower. Alpha abundance, speed, and temperature measurements suggest that the SB intervals are more like *fast wind*. Panel (g) demonstrates that the set of structures is in local pressure balance consistent with spatially stable structure on the spacecraft transit timescale.

enhancements are also measured for some of these intervals (panel (c)). It has been reported previously that the Alfvénic magnetic field SBs are interspersed in regions of *quiet radial flow* (Bale et al. 2019; Horbury et al. 2020); here, at $20 R_S$ they are clearly modulated periodically and in correspondence with field amplitude and proton radial flow. Along the bottom of Figure 2 the spacecraft position in Carrington (HG) longitude is shown, as mapped ballistically using the measured proton speed (e.g., Nolte & Roelof 1973; Badman et al. 2020). The time interval of the modulated features (red arrows) corresponds to Carrington

longitudes of $\sim\!\!250^\circ\!\!-\!\!270^\circ$ in Figure 1. The modulations of SBs and plasma parameters occur on angular scales of a few degrees, similar to the network magnetic field and supergranulation scales on the Sun as in Figure 1.

Figure 3 highlights the interval of modulated SBs between 2020 September 27/01:00:00 and 2020 September 28/08:00. The top panel shows ion flux measurements from ISOIS in three energy channels from the EPI-Lo time-of-flight (TOF) system between 30–84 keV. An examination of the triple coincidence data shows that these TOF-only measurements are likely to be

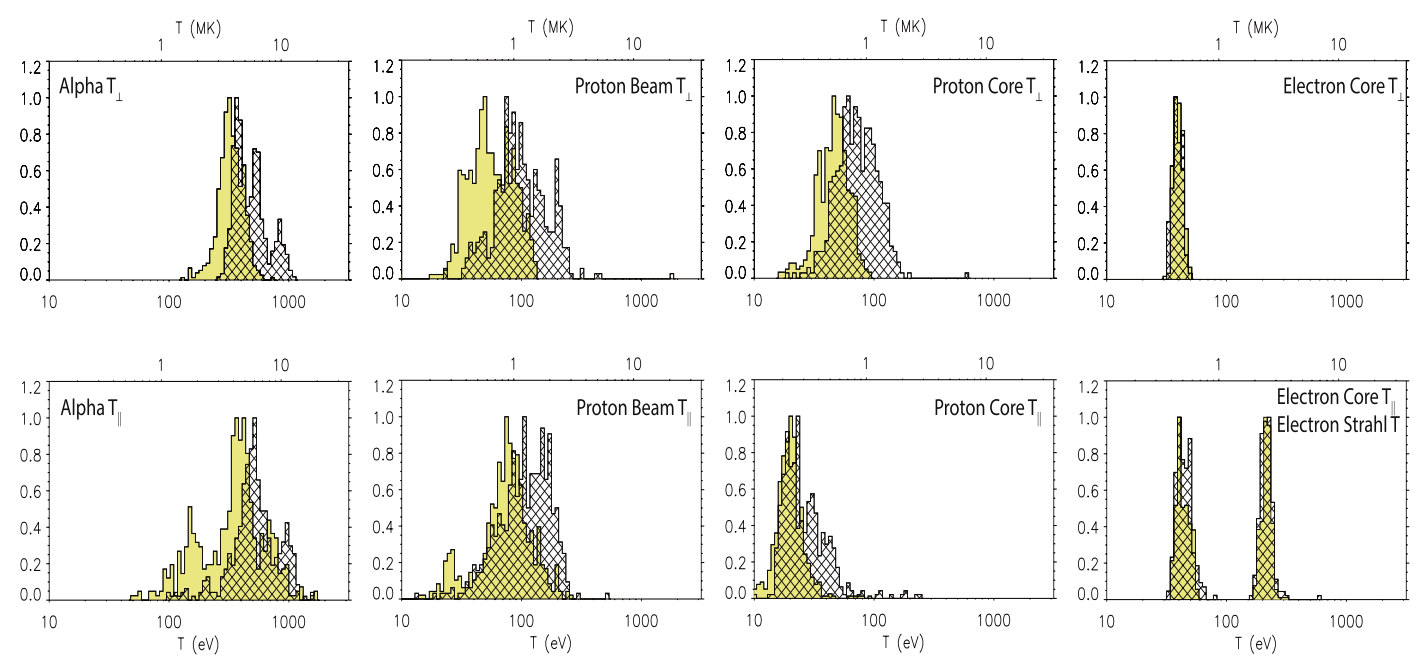


Figure 4. Distribution of temperatures (normalized with the peak to one) for alpha particles, beam protons, core protons, and core and strahl electrons, both perpendicular to the magnetic field (upper row) and parallel (lower row). The hatched histograms are within the funnel structures and the beige histograms are outside of the funnels. Temperatures are given in electronvolts (lower axis) and millikelvin (upper axis). Protons and alpha particles are all hotter within the funnel structures, as seen in Figure 3 as well. Electron T_{\perp} is similar inside and out, with electron T_{\parallel} slightly enhanced within the funnels. Characteristic values are given in Table 1.

dominated by a mix of He and/or O ions and are field aligned (anti-sunward). Note that these suprathermal ions appear most clearly within the last two modulations (in yellow bars), which also contain higher speed flow (panel (e)), suggesting that these ions may be the suprathermal tail of the modulated solar wind distribution. Panel (b) is the measured alpha particle abundance $A_{\rm He} = n_{\rm o}/n_{\rm total}$ showing strong modulations to relatively large values (~4%) associated with the SB patches and magnetic field amplitude modulations in panel (c). The dashed line in panel (c) indicates the nominal heliospheric field of 2.5 nT au² (Badman et al. 2021) and the depressed intervals are colored blue. Light yellow vertical panels indicate intervals with enhanced $A_{\rm He}$ and depressed |B|. Alpha particle temperature T_{α} (green) and proton core temperature T_p (red) are enhanced within these intervals and electron core (lower blue) and strahl (upper blue) temperatures are depressed; note that $T_{\alpha}/T_{p} \approx 4-15$ as will be discussed below. Plasma radial velocities (panel (e)) are enhanced within the structures with the core proton speed (blue) approaching the Alfvén speed (black) on the edges and Alfvén Mach $M_A \approx 2$ within. The alpha (green) and proton beam (red) speeds are a large fraction of an Alfvén speed. The inverse correlation of electron temperature to wind speed $T_e \propto 1/v_{\rm sw}$ is well known and observed quite universally during PSP solar encounters (e.g., Maksimovic et al. 2020).

Panel (f) in Figure 3 show the number flux of core protons (blue), beam protons (red), and alpha particles (green). The core proton flux is relatively steady, while the proton beam and alpha particle flux are more modulated by the plasma structure; the proton beam abundance (not shown) is not so clearly modulated, rather the proton beam speed is enhanced within the high-alpha abundance structures. Magnetic field pressure (black) and plasma pressure are shown on panel (g), with proton (red), core electron (blue), and alpha (green) all showing anticorrelation with the magnetic field pressure. This is best seen in panel (h) where the total pressure (magnetic plus plasma) is shown, normalized to a slowly varying factor to remove the large-scale radial trend—

these structures are in local pressure balance. Pressure-balanced structure (PBS) is seen throughout the solar wind in the inner heliosphere (Thieme et al. 1990), at 1 au (Borovsky 2016), and on Ulysses (McComas et al. 1995, 1996) and Reisenfeld et al. (1999) reported an association between PBS and enhanced alpha particle abundance. Here, we take this as evidence that these structures are spatial and stable over the spacecraft transit time, at least. The lower panel shows plasma β for proton (red), alphas (green), and electrons (blue) demonstrating the ion β is enhanced inside the structures. In addition to the measurements shown in Figure 3, these intervals show modulations of the proton core temperature anisotropy T_{\perp}/T_{\parallel} that often exceed the anisotropy-driven ioncyclotron instability threshold (e.g., Hellinger et al. 2006), relatively large proton beam speeds and alpha-proton drifts (comparable to v_A) and depressed T_e/T_p and the interval is richly populated with ion-cyclotron-frequency waves (Bowen et al. 2020; Verniero et al. 2020). Enhanced proton-alpha drifts within PBSs have been reported previously by Yamauchi et al. (2004). The kinetic features measured here are also associated with enhanced electrostatic plasma waves and will be investigated more fully in a future study.

In summary, Figure 3 demonstrates that PSP is transiting over spatial plasma structures that are a few degrees of HG longitude across mapped to the Sun. The structures contain hotter and faster ions (protons and alpha particles), a markedly enhanced alpha particle abundance $A_{\rm He}$, suprathermal ions, depressed magnetic field |B| and electron temperature T_e , and a clear increase in the amplitude and occurrence of magnetic field SBs. Since the alpha abundance, and arguably the electron temperature, are frozen-in from the solar wind source in the transition region, we argue that the suprathermal ions have an origin at these altitudes and that the physics of these solar wind sources organizes the spatial and temporal distribution of the SBs.

Histograms of ion and electron temperatures are shown in Figure 4, normalized to unity maximum and characteristic

Table 1
Average, Mode, and Standard Deviation of the Distribution of T_{\perp} and T_{\parallel} in Units of Electronvolts, Inside and Outside of the Funnel Structures (Inside/Outside)

	inside/outside			inside/outside		
Species	$\langle T_{\perp} angle$	$Mo(T_{\perp})$	$\sigma(T_{\perp})$	$\langle T_{ } angle$	$Mo(T_{\parallel})$	$\sigma(T_{\parallel})$
He ⁺⁺	501/335	360/305	171/79	570/400	464/340	247/241
Beam H ⁺	114/60	75/47	96/25	117/81	105/74	54/40
Core H ⁺	78/47	58/40	37/13	30/21	17/21	23/8
Core e	39/40	36/39	6.2/6.3	45/43	39/41	6.7/6.6
Strahl e	n/a	n/a	n/a	217/215	216/220	15/15

values are collected in Table 1. The cross-hatched histograms are accumulated within the high-alpha structures and the beige histograms are from outside the structures. The proton and alpha populations are generally hotter within the magnetic structures, while both core and strahl electrons are slightly cooler, reminiscent of fast solar wind. Variations from structure-to-structure mask some of the trends in the unnormalized temperature that become more apparent in the dimensionless ratios in Figure 5.

Stansby et al. (2019b) compared Helios measurements of alpha and proton temperatures down to 0.3 au to expectations from double-adiabatic theory (Chew et al. 1956) (or CGL). They found that $T_{\alpha,\parallel}$ decreases faster with radial distance than predicted by CGL, while $T_{\alpha,\perp}$ decreases more slowly, consistent with isotropization associated with temperature anisotropy instabilities (Hellinger et al. 2006; Bale et al. 2009; Maruca et al. 2012). Our average values within the funnel intervals at $\sim 20R_S$ (~ 0.1 au) of $\langle T_{\alpha,\parallel} \rangle \approx 570 \,\text{eV}$ (6.6 MK), $\langle T_{\alpha,\perp} \rangle \approx 501 \,\text{eV}$ (5.8 MK), $\langle T_{\rho,\parallel} \rangle \approx 30 \,\text{eV}$ (0.35 MK), and $\langle T_{\rho,\perp} \rangle \approx 78 \,\text{eV}$ (0.9 MK) are consistent with the trends in Figure 1 of Stansby et al. (2019b) and $\langle T_{\alpha,\perp} \rangle$ seems to trend with their CGL curve. In Figure 5 we show the distribution of relative (to proton core) temperatures (top panel) and the temperature anisotropy T_{\perp}/T_{\parallel} for each population, over the interval. Notably, the alpha particles are heated substantially relative to the core protons with T_{α} peaking near $T_{\alpha} \sim 8$ $T_{p,c}$, well above, even twice, the mass-proportional heating $T_{\alpha} \sim 4$ $T_{p,c}$ rate. More-than-mass-proportional heating has been measured in the inner heliosphere previously (Marsch et al. 1982; Gershman et al. 2012), and at 1 au (Kasper et al. 2017) and here we identify it with discrete solar wind sources and report, we believe, one of the largest ever heating fractions $T_{\alpha} \gtrsim 10$ $T_{p,c}$ for thermal alpha particles in the solar wind. Notably, there is no thermalized population $T_{\alpha} \sim T_p$. Indeed, Maruca et al. (2013) used measurements of T_{α}/T_{p} at 1 au and a model of collisional evolution to infer large temperature ratios in the inner heliosphere; their model removed the 1 au isotropic population $T_{\alpha} \sim T_p$ and the distribution was predicted to peak at $T_{\alpha} \sim 5.4 T_p$ at 0.1 au ($\sim 21 R_s$). If robust and general, our results imply source of isotropization in addition to collisions, presumably wave-particle effects (e.g., Klein et al. 2018). Note that alpha-to-proton temperature ratios of \sim 10 were predicted at 15 R_S by Chandran (2010) based on stochastic ion heating by low frequency MHD/kinetic Alfvén wave turbulence.

The proton beam population is heated to $T_{p,b} \sim 2T_{p,c}$, while the core electrons are cooler than the core protons $T_{e,c} \lesssim T_{p,c}$ as observed for faster solar wind sources (Marsch et al. 1989; David et al. 1998; Maksimovic et al. 2020). The lower panel of Figure 5 shows the temperature anisotropy T_{\perp}/T_{\parallel} of the core electron (blue), core proton (green), beam proton (red), and alpha particle (black) populations. The core proton population is notably more anistropic; the proton beam and alpha particle populations show similar distributions of temperature anisotropy. This may be a

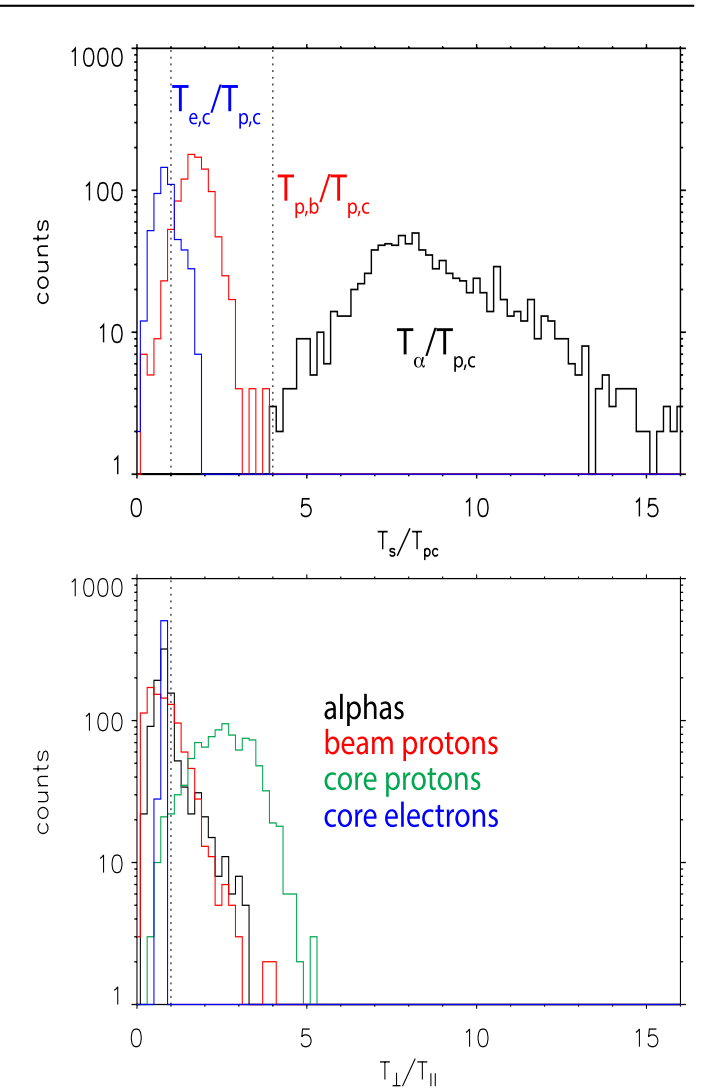


Figure 5. Distribution of temperatures (upper panel) and temperature anisotropy (low panel) for alpha particles (black), beam protons (red), core protons (green), and core electrons (blue). The alpha particle total temperature shows clear evidence of heating above mass ratio $T_{\alpha}/T_{p,c} > m_{\alpha}/m_p = 4$ and peaks near $T_{\alpha}/T_{p,c} \approx 8$. The distribution of proton beam temperatures peaks at near $T_{p,b}/T_{p,c} \approx 2$ and the core electron population is slightly cooler than the protons $T_{e,c}/T_{p,c} < 1$. While the core protons are strongly anisotropic $T_{\perp}/T_{\parallel} \geqslant 2$, the alpha particles, beam protons, and electrons all show slightly enhanced parallel temperatures $T_{\perp}/T_{\parallel} \lesssim 1$. Note that the distributions of alpha and beam proton temperature anisotropies are very similar suggesting a common heating and/or evolution mechanism.

result of a common heating or energization mechanism, or rather may indicate similar physics during radial evolution. Since the beam protons and alpha particle stream ahead of the core protons, these populations will interact differently with Alfvénic fluctuations propagating in the wave frame with respect to the bulk (core proton) solar wind.

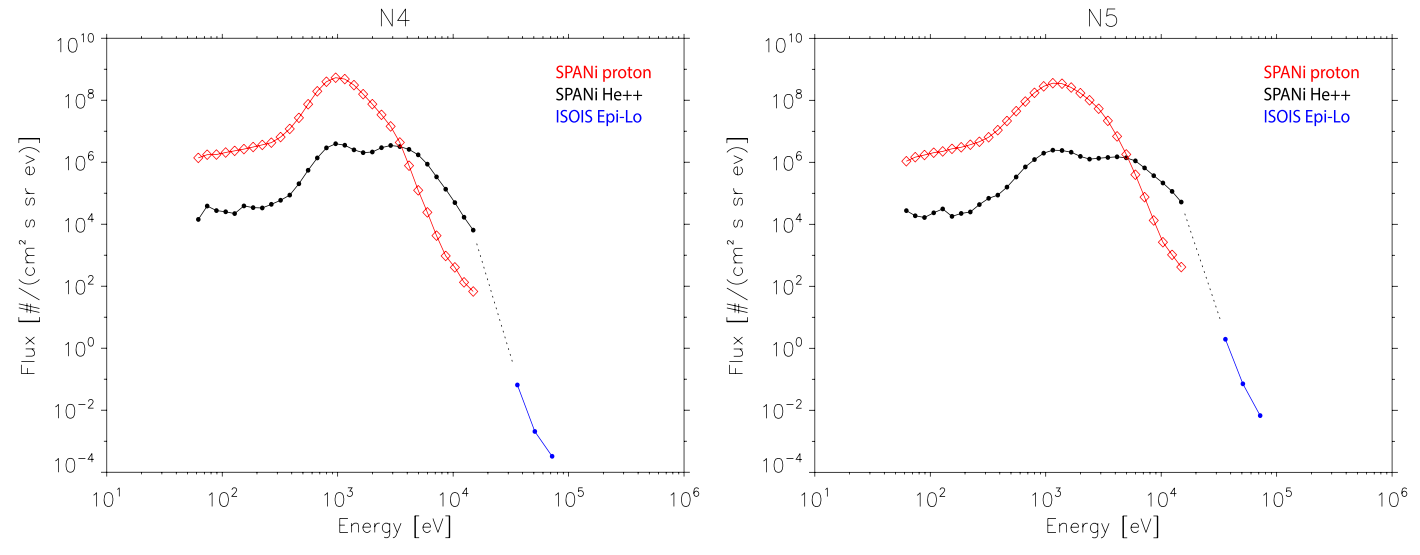


Figure 6. Energy spectra in units of differential number flux during the interval within the last two yellow-highlighted funnel structures of Figure 7 (labeled N4 and N5 there). A dotted line with spectral index ~ -11 extends between the SPANi alpha and ISOIS measurements; we suggest that the ISOIS ions are the suprathermal tail of the solar wind alpha spectrum.

Figure 6 shows energy spectra of protons and alpha particles measured by SPANi compared with the ISOIS EPI-Lo spectrum; these spectra are in units of differential number flux j and averaged over the intervals 2020 September 27/21:28:00-2020 September 28/00:10:00 (left) and 2020 September 28/ 02:44:30-2020 September 28/04:55:30 (right), corresponding to the final two yellow boxes in Figure 3 and labeled N4 and N5 in Figure 7. The ISOIS suprathermal spectrum is shown assuming a spectrum of He⁺⁺ (as described above); if the ISOIS spectrum is oxygen the fluxes will be a factor of 4 higher. While suprathermal He⁺⁺ is observed routinely in the ecliptic, slow solar wind (e.g., Collier et al. 1996) most usually associated with shocks or corotating interaction regions (or pickup ions), Ulysses measurements show a negligible ambient suprathermal He⁺⁺ population in the fast solar wind (Gloeckler & Geiss 1998). Our measurements here, with the striking correlation in Figure 3 and the plausible continuity of the spectrum in Figure 6, suggest that the EPI-Lo ion measurements are the tail of a very steep alpha particle spectrum out to 85 keV. A dotted line in Figure 6 connects the SPANi and EPI-Lo spectra and has a spectral slope $j \sim E^{-11}$. There is no notable radio emission nor flaring activity at this time.

To infer the spatial structure at the origin, we project the PSP spacecraft location in HG longitude down to the solar surface using a ballistic mapping (Nolte & Roelof 1973; Badman et al. 2020) in Figure 7. The T, N-plane magnetic field (upper panel) and proton velocity (lower panel) vectors are computed as 10 minute statistical mode values, in an attempt to remove the dominant and rapidly varying SB fields. A time series plot (not shown) suggests that this is largely successful and the vectors shown here represent larger scale deviations of the underlying field and flow. Where no vector is apparent, the flow/field is primarily radial. The vectors are centered on the spacecraft coordinates—note that the spacecraft latitude is not corrected for ballistics or footpoint location and as shown in Figure 1 the local magnetic field footpoint ultimately maps to southern HG latitudes of around -60° . The time series measurements of the plasma and magnetic field are overplotted in their ballistically propagated HG longitude coordinates (and in arbitrary units here). The result of the ballistic backprojection shows that the sources are highly structured and steepened at the leading edge; the smooth profile at PSP altitudes is a result of TOF. The intervals with enhanced $A_{\rm He}$ are colored yellow and labels N1–N5. The SB intervals (red bars $B_{R,{\rm Max}}$ and $V_{R,{\rm Max}}$) cluster near the leading edge or just within. Magnetic field intensity |B| and electron temperature T_e are just inside this boundary; we will suggest below that this minimum in magnetic field and electron temperature correspond to the central region of an asymmetric magnetic structure.

It is interesting to note that for the last three events here (N3–N5), there appears to be a small (\sim 1°) leading edge (in the spacecraft frame) interval for which the maximum radial field and speed ($B_{R,\text{Max}}$ and $V_{R,\text{Max}}$) leads the step in the minimum values $B_{R,\text{Min}}$ and $V_{R,\text{Min}}$. These intervals (colored light blue in Figure 7) also correspond to decreasing trends in |B| and T_e and enhanced proton core temperatures T_{\parallel} and T_{\perp} . Similar structure was measured at stream interface boundaries with instruments on the Helios spacecraft in the inner heliosphere (Marsch et al. 1982).

Figure 8 shows some data from Figure 7 represented in polar coordinates (i.e., in the plane of the HG ecliptic). While the information here is equivalent to Figure 7, the polar representation emphasizes the angular extent of these structures on the Sun and the potential relationship to the underlying photospheric structure.

3. Interpretation and Discussion

To summarize the observations in the previous section, our measurements show the following:

- (i) PSP passed through a \sim 34 hr interval of modulated magnetic field SBs and ion and electron flux. This interval corresponds to \sim 25° of HG longitude at the Sun during which PSP was magnetically connected to a CH boundary near -60° HG latitude. The spacecraft was below 25 R_S .
- (ii) The modulations correspond to angular scales of 3°-5° in HG longitude at the Sun—similar to the supergranulation and network magnetic field structure. PFSS-mapped

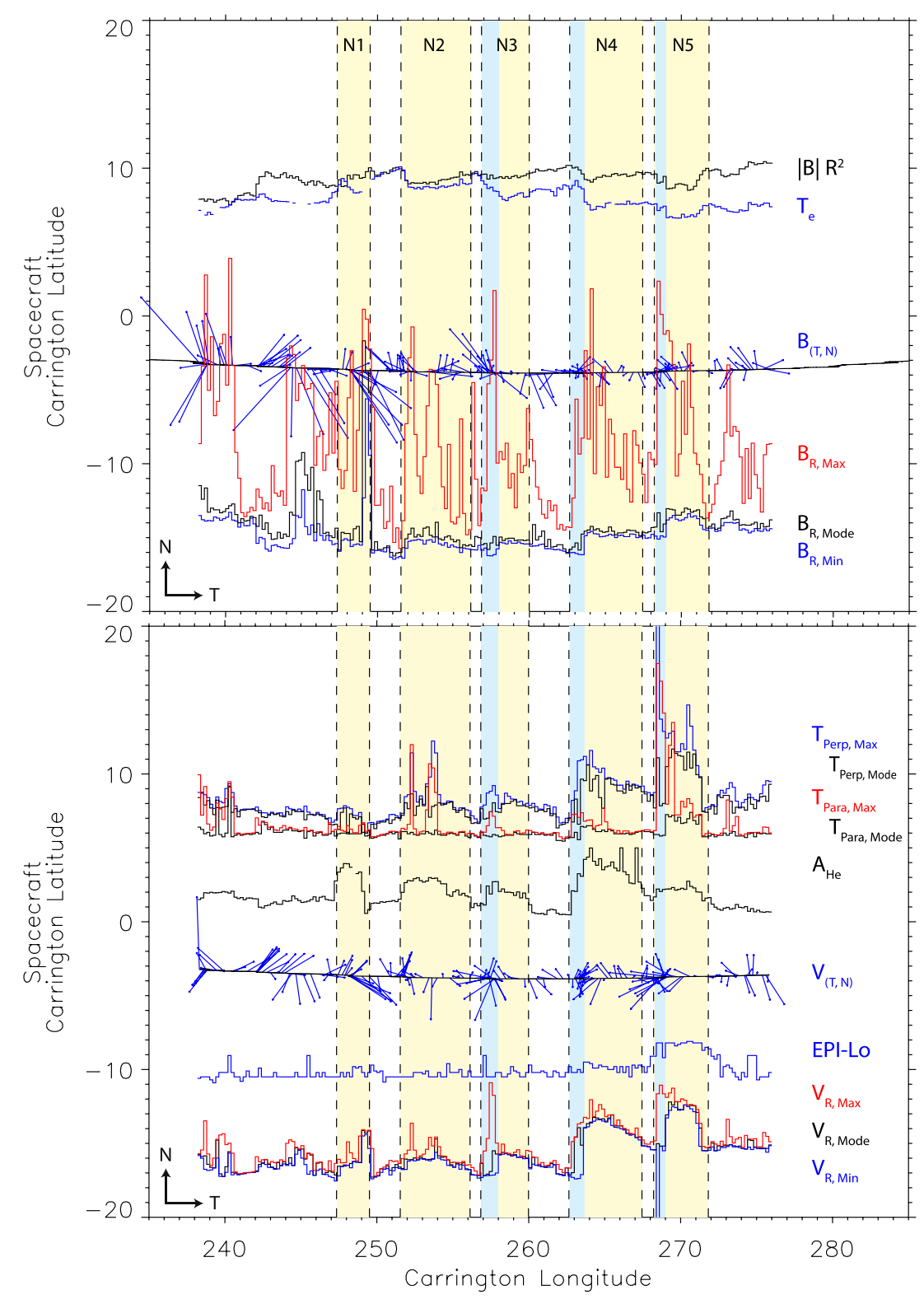


Figure 7. Magnetic field (upper panel) and proton velocity (lower panel) vectors in the T-N plane and centered on the spacecraft position in latitude and ballistically mapped Carrington longitude. Field magnitude $|B|R^2$, electron core temperature T_e and radial field B_R (upper panel) and proton T_\perp and T_\parallel , $A_{\rm He}$, and radial core proton speed V_R (lower panel) are overplotted in arbitrary units. Maximum, minimum, and mode values are shown for B_R and V_R and maximum and mode for the proton temperatures. Data are accumulated in bins of $0^{\circ}2$ longitude. Yellow vertical bars show intervals (labeled N1-N5) of enhanced $A_{\rm He}$ within the PBS and blue vertical bars indicate subintervals with enhanced temperature and radial flow. The T-N plane field and velocity vectors show non-radial structure near the boundaries of the $A_{\rm He}$ enhancements. $A_{\rm R,Max}$ (red bars, upper panel) indicates the distribution of SBs; occurrence and amplitude is organized by the PBS and peaks near, but somewhat within, the leading edge at the source on the Sun. Intervals of enhanced proton T_{\parallel} , radial speed, and electron temperature T_e occur within $\sim 1^{\circ}$ of the (spacecraft frame) leading edge of structures N3-N5.

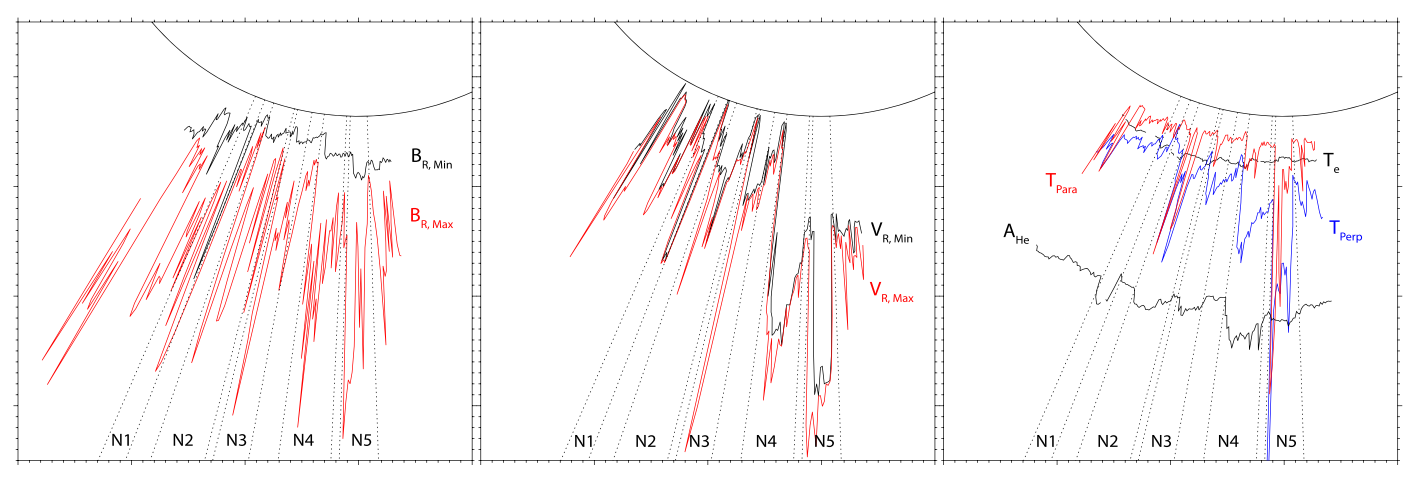


Figure 8. Polar representation of the data from Figure 7 with the noted parameters in arbitrary units. This shows clearly the longitudinal structure and angular scale of the sources. The solar rotation is counterclockwise. The structures show steep leading edge features in magnetic field intensity, radial proton speed, and proton T_{\perp} ; proton T_{\parallel} is peaked sharply near the leading edge of events N2–N5.

footpoints show magnetic field concentrations on similar angular scales.

- (iii) The modulated intervals are in total pressure balance implying that the structures are spatial on the spacecraft transit timescale (∼6 hr).
- (iv) The thermal alpha particle abundance $A_{\rm He}$ is enhanced to typical fast wind values and the core and strahl electron temperatures are depressed within the modulations, implying solar wind sources on open field lines at the base of the corona similar to fast CH wind.
- (v) Proton and alpha particle radial speeds and temperatures and ion plasma β are enhanced within the structures. Alpha particles and beam protons are streaming ahead of the core protons and their number flux is strongly modulated by the structures. The alpha particles are $\sim 5-15\times$ hotter than the core protons. The alpha particles are fairly isotropic $T_{\perp}/T_{\parallel}\lesssim 1$, while the core protons have $T_{\perp}/T_{\parallel}>1$ and are often unstable to an anisotropy-driven ion-cyclotron instability.
- (vi) Suprathermal ions with energies up to ~85 keV are measured within a subset of the structures with higher bulk velocities, suggesting a suprathermal tail. There is no notable radio emission nor TOF dispersion that suggests a classical flare origin of the suprathermal ions. We suggest that PSP is transiting field lines populated by these ions.
- (vii) When mapped ballistically to the solar surface, the structures have a steep leading edge at lower Carrington/HG longitude. This may be a signature of a some small differential rotation between the photosphere and the corona (photosphere moving faster) or maybe be some inherent asymmetry of the source fields at the CH boundary. The SBs cluster near the steep edge of the structures.
- (viii) A narrow $\sim 1^{\circ}$ region is found at the (spacecraft frame) leading edge of the steepest structures that has enhanced proton and alpha temperatures T_p , T_{α} , large differences between maximum and minimum radial field and flow, and a transition of |B| and T_e .

An enhanced relative abundance of alpha particles $A_{\rm He} = n_{\alpha}/n_{\rm tot}$ is known to be associated with fast solar wind, especially during solar minimum conditions (e.g., Kasper et al. 2012). Since the alpha abundance $A_{\rm He}$ is determined in the

chromosphere or transition region our measurements suggest a direct mapping to discrete solar wind sources. The modulation of wind speed and alpha abundance A_{He} on the angular scales of solar supergranulation strongly implies that these microstreams originate within the network magnetic field that is known to cluster at the boundaries of the supergranules (viz. Rieutord & Rincon 2010; Wiegelmann et al. 2014). Theoretically this was suggested as the source of the fast solar wind in the furnace model of Axford et al. (1999). Open field lines containing hot plasma pass through the solar transition region and overexpand rapidly, as the high-order magnetic field falls off radially much more rapidly that the plasma pressure. The resulting magnetic funnel structures (Gabriel 1976, 1977; Dowdy et al. 1986; Axford et al. 1999; Hassler et al. 1999; Tu et al. 2005) then expand into pressure balance to generate solar wind. Our measurement of magnetic field intensity depressions within the structures is consistent with the overexpansion of magnetic funnels, as the axial field should decay as $B_R \sim 1/A$ while $B_{T,N} \sim 1/\sqrt{A}$ with A the flux tube area, so that magnetic field at the center of the funnel (the axial, more radial component) will be weaker after expansion. The magnetic funnels expand rapidly at low altitudes and reconnection of impinging small dipoles and emerging flux are the source of energy generating the solar wind within the larger CH structure, whose speed is determined by the overall expansion at higher altitude, found to be anticorrelated with the asymptotic solar wind speed Wang & Sheeley (1990); a two-step expansion process has been explored by Suess et al. (1998) and others.

The association of large-amplitude, nonlinear Alfvénic fluctuations (i.e., the SBs), enhanced bulk flow, and more-than mass-proportional ion heating with the edge of the funnel structure suggests an asymmetry in the source region that is associated with the heating. Figure 9 is a schematic of the magnetic field structure at the source. The field vectors here are a 2D potential model of a magnetic funnel (Hackenberg et al. 1999) as a set of unipolar flux concentrations and a dipole field with a shear in the $-\hat{x}$ direction; color intensity in Figure 9 is magnetic field magnitude.

The enhancement of SBs in wind emanating from funnel boundaries clearly demonstrates the impact of structure and processes near the Sun on the spatial distribution of SBs in the solar wind. In particular, the enhanced values of δB_R in these

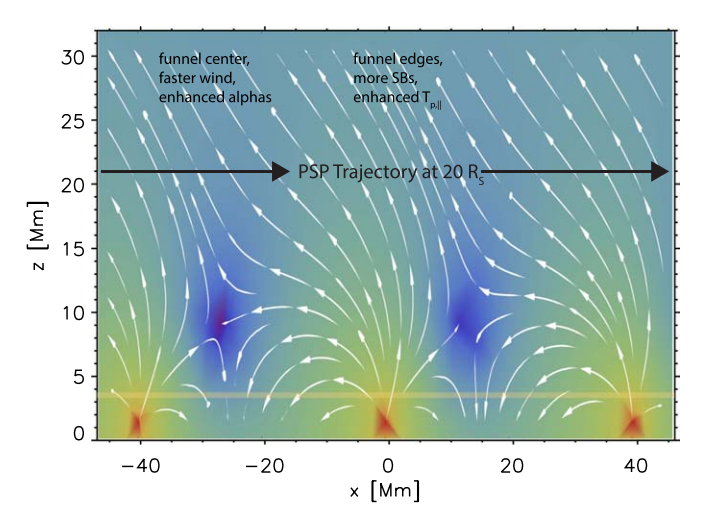


Figure 9. A schematic to illustrate the proposed configuration of magnetic field lines (white vectors) within overexpanded funnel structure and a small shear between the photosphere and corona. The color intensity indicates field magnitude. The bases of the funnels are separated by a few degrees of HG longitude and are generating higher β wind with enhanced alpha particle abundance. Patches of magnetic field SBs are localized within the funnels. Since $B_R \sim 1/r^2$, but $B_{(T,N)} \sim 1/r$, super-radial expansion results in a depressed |B| in the center of the funnel, which has spent more time expanding radially. In this 2D geometry, the *cusp* regions (darker blue) where neighboring funnels interact moves to lower altitudes with increasing shear; note that the cusp intervals are ~ 10 Mm-scale, which corresponds to $\sim 1^\circ$. A horizontal band indicates the transition region. Note that the local funnel geometry can be expanded away by $20 R_S$.

regions is strong evidence of preferential Poynting-flux injection near funnel boundaries in the low solar atmosphere, which could be the result of magnetic reconnection. It is possible that the Poynting-flux injection is not only stronger but also more intermittent near funnel boundaries, since reconnection is often impulsive. However, as noted previously, large-amplitude magnetic fluctuations in the solar wind naturally develop discontinuities as a consequence of spherical polarization (e.g., Vasquez & Hollweg 1996; Squire et al. 2020; Shoda et al. 2021), and thus the abrupt magnetic field rotations observed by PSP may also originate through in situ dynamics.

The cores of the funnels are separated by 40 Mm (\sim 3°.3) here and already at 30 Mm altitude the field direction becomes relatively uniform, but is modulated in intensity as described above due to the super-radial expansion below. The low altitude cusp regions (shaded dark blue in Figure 9) where adjacent funnels interactions result in an x point (in 2D) with a spine-fan intersection and a dome of confined flux, where magnetic reconnection could leak heated and confined plasma outward. This asymmetry is seen in the hotter, faster leading edge of the measurements in Figure 7. Indeed, simulations of reconnection between funnels and emerging flux show this asymmetry (Jiang et al. 2012; Takasao et al. 2013) and the resulting outflows depend on the altitude of the reconnection region. Here, the cusp regions move to lower altitude with increasing (applied) magnetic shear (\hat{x} component); magnetic shear could be due to differential rotation between the photosphere and corona or a property of the structure of the CH boundary.

Magnetic reconnection may also naturally explain the energization of alpha particles (or oxygen) to 85 keV and the altitude of a reconnection site may be related to alpha particle abundance, if gravitational settling plays a role. If the full magnetic energy of a reconnection outflow is available to

energize alpha particles (e.g., Phan et al. 2013), we can infer the Alfvén speed at the source $\frac{1}{2}m_{\alpha}v_{A}^{2}\sim85$ keV, which gives $v_{A}\sim2020\,\mathrm{km\,s^{-1}}$, not inconsistent with expectations at low altitudes (e.g., Axford et al. 1999; Warmuth & Mann 2005). Drake et al. (2009) describe simulations of an ion pickup process in reconnection outflow regions that effectively energizes alpha particles to $\sim \frac{1}{2}m_{\alpha}v_{A}^{2}$.

energizes alpha particles to $\sim \frac{1}{2} m_{\alpha} v_A^2$. Spectroscopic measurements deep into the solar wind acceleration region show that minor ions (e.g., O5+) are heated and accelerated to much higher energies than the bulk proton population (e.g., Kohl et al. 1998; Cranmer et al. 1999) and that that heating is a function of altitude, suggesting that waveparticle processes are at play during expansion. Indeed, Kasper et al. (2013) used measurements at 1 au to show that alpha particle temperature statistics are consistent with ion-cyclotron heating. A recent model (Meyrand et al. 2021: Squire et al. 2021) suggests that imbalanced Alfvénic turbulence evolves to enhanced ion-cyclotron wave energy as a helicity barrier inhibits turbulent evolution beyond the ion scales and this results in enhanced ion heating. So while many of our measurements are consistent with an impulsive heating mechanism at the source. wave-particle effects during radial evolution may certainly play a role in the observed ion temperature statistics.

The observation that the lower-|B| funnels are replete with SBs is consistent with the theory that SBs grow as a consequence of Alfvénic fluctuations reaching large amplitudes through solar wind expansion (Squire et al. 2020; Mallet et al. 2021). Specifically, funnel regions have presumably undergone more super-radial expansion than neighboring regions, so even minor variations in relative fluctuation amplitudes at the SS could lead to large differences at the location of PSP (Hollweg 1974). Fluctuations that grow to $\delta B/B \gtrsim 1$ then form SBs or potentially flux ropes associated with turbulent reconnection (e.g., Drake et al. 2021). The relation of this to other solar wind properties (wind speed, proton temperature, and alpha fraction) remains an open problem: the funnels described here lead to solar wind streams dubbed Alfvénic slow streams (Stansby et al. 2019a; D'Amicis et al. 2021), rather than the fast wind typically associated with polar CH outflows. The reason is that the speed of the solar wind is controlled not by the local expansion discussed here occurring within 20 Mm from the photosphere, but the overall CH expansion. PSP, always skirting the current sheet in the ecliptic plane as the Sun's activity picks up out of the latest minimum, has been mostly observing wind coming from rapidly expanding open field lines. For this type of wind, the heating and acceleration is similar to fast solar wind (Chandran 2021), including plasma properties, but the global coronal geometry determines the slower acceleration profile (Wang & Sheeley 1990; Panasenco et al. 2019).

The stream structure and fluctuations shown here must evolve to become the familiar solar wind at 1 au and beyond. T. S. Horbury et al. (2021, in preparation) used measurements by Solar Orbiter of the same solar wind stream at $200 R_S$ as presented here: while the alpha particle modulation was preserved, the longitudinal speed variations were smoothed out by that distance, leading to density variations on the same longitudinal scale. The clear variation in fluctuation power due to SB modulation that was present at $25 R_S$ was replaced by a large-scale magnetic field variation on the same scale, suggesting that the photospheric structure affecting the wind at PSP still retains a signature in the wind much farther from the Sun.

Coronal magnetic activity is naturally multiscale. Large-scale activity (e.g., flares and coronal mass ejections) correlate well with the sunspot solar cycle, while smaller-scale activity (e.g., bright points, plumes, and jets) is more ubiquitous regardless of the solar cycle phase. Space and ground-based observations in the 1970s provided the first evidence for the highly dynamic nature of the coronal base (Demastus et al. 1973; Bohlin et al. 1975; Withbroe et al. 1976; Brueckner 1980). Yohkoh/SXT observations showed most energetic coronal jets (e.g., Shibata et al. 1992; Strong et al. 1992; Shimojo et al. 1996, 1998, 2001). These discoveries led to speculations on the role these transients play in the heating and acceleration of the solar wind plasma (Brueckner & Bartoe 1983).

Our in situ measurements imply a connection between impulsive Alfvénic activity within discrete wind sources and solar wind heating and acceleration mechanisms. While our measurements appear to be consistent with interchange reconnection, either through direct heating from the reconnection site itself or through enhanced Poynting fluxes (e.g., waves) that dissipate at higher altitudes, there are other viable mechanisms to consider. Axford et al. (1999) describe a wave-heating process occurring within magnetic funnels: high frequency Alfvén waves propagating outward enter resonance with ions and heat perpendicular to the local magnetic field and the resulting mirror force produces accelerated flow (Czechowski et al. 1998); resonant ion-cyclotron heating is observed at 1 au (Kasper et al. 2013). Martinez-Sykora et al. (2017) suggest that ambipolar diffusion transports kinked field lines near network field concentrations into the chromosphere and the stored magnetic tension is released impulsively to form type II spicules and Alfvénic jets.

Finally, it is interesting to speculate about a connection to coronal plumes—persistent filamentary structures that disappear into the general solar wind outflow several tens of solar radii above the Sun's surface (DeForest et al. 1997; Teriaca et al. 2003; Wang & Muglach 2008; Wilhelm et al. 2011; Yu et al. 2014; Poletto 2015; Raouafi et al. 2016). Plumes are also known to emerge from network field concentrations with enhanced heating at the base and are characterized by higher density (Wang 1994) and lower electron temperatures (DeForest et al. 1997) than the surrounding corona. Raouafi et al. (2008) show that coronal plumes display myriads of small, short-lived jets at their footpoints (Raouafi & Stenborg 2014), most probably resulting from magnetic reconnection due to small emerging bipolar features (see, e.g., Panesar et al. 2018, 2019). Plumes exhibit oscillations and substructures (Uritsky et al. 2021) and should expand in pressure balance into the solar wind (Velli et al. 2011), but their potential relationship to the structures observed by PSP and reported here remains to be explored.

Parker Solar Probe was designed, built, and is now operated by the Johns Hopkins Applied Physics Laboratory as part of NASA's Living with a Star (LWS) program (contract NNN06AA01C). Support from the LWS management and technical team has played a critical role in the success of the Parker Solar Probe mission. We would like to acknowledge the efforts of the FIELDS, SWEAP, and ISOIS instrument and science operations teams and the PSP spacecraft engineering and operations team at the Johns Hopkins Applied Physics Laboratory. O. Panasenco was supported by the NASA grant 80NSSC20K1829. M.V. was partially supported by the HERMES DRIVE NASA Science

Center grant No. 80NSSC20K0604. B.C. was supported by NASA grants NNX17AI18G and 80NSSC19K0829. J.S. was supported by the Royal Society Te Aparangi NZ through Rutherford Discovery Fellowship RDF-U00180. T.H. and L.W. were supported by UK STFC grant ST/S000364/1, T.W. by ST/T506151/10 and R.L. by an Imperial College President's scholarship. J.F.D. was partially supported by the NASA DRIVE Science Center on Solar Flare Energy Release, grant No. 80NSSC20K0627 and NSF grant No. PHY2109083.

ORCID iDs

```
S. D. Bale https://orcid.org/0000-0002-1989-3596
T. S. Horbury https://orcid.org/0000-0002-7572-4690
M. Velli https://orcid.org/0000-0002-2381-3106
M. I. Desai https://orcid.org/0000-0002-7318-6008
J. S. Halekas https://orcid.org/0000-0001-5258-6128
M. D. McManus https://orcid.org/0000-0001-6077-4145
O. Panasenco https://orcid.org/0000-0002-4440-7166
S. T. Badman https://orcid.org/0000-0002-6145-436X
T. A. Bowen https://orcid.org/0000-0002-4625-3332
B. D. G. Chandran https://orcid.org/0000-0003-4177-3328
J. F. Drake https://orcid.org/0000-0002-9150-1841
J. C. Kasper https://orcid.org/0000-0002-7077-930X
R. Laker https://orcid.org/0000-0002-6577-5515
A. Mallet https://orcid.org/0000-0001-9202-1340
T. D. Phan https://orcid.org/0000-0002-6924-9408
N. E. Raouafi https://orcid.org/0000-0003-2409-3742
J. Squire https://orcid.org/0000-0001-8479-962X
L. D. Woodham https://orcid.org/0000-0003-2845-4250
T. Woolley https://orcid.org/0000-0002-9202-619X
```

References

```
Altschuler, M. D., & Newkirk, G. 1969, SoPh, 9, 131
Axford, W. I., McKenzie, J. F., Sukhorukova, G. V., et al. 1999, SSRv, 87, 25
Badman, S. T., Bale, S. D., Martínez Oliveros, J. C., et al. 2020, ApJS, 246, 23
Badman, S. T., Bale, S. D., Rouillard, A. P., et al. 2021, A&A, 650, A18
Bale, S. D., Badman, S. T., Bonnell, J. W., et al. 2019, Natur, 576, 237
Bale, S. D., Goetz, K., Harvey, P. R., et al. 2016, SSRv, 204, 49
Bale, S. D., Kasper, J. C., Howes, G. G., et al. 2009, PhRvL, 103, 211101
Balogh, A., Forsyth, R. J., Lucek, E. A., Horbury, T. S., & Smith, E. J. 1999,
      RL. 26, 631
Bohlin, J. D., Vogel, S. N., Purcell, J. D., et al. 1975, ApJL, 197, L133
Borovsky, J. E. 2016, JGRA, 121, 5055
Bowen, T. A., Mallet, A., Huang, J., et al. 2020, ApJS, 246, 66
Brueckner, G. E. 1980, ApOpt, 19, 3994
Brueckner, G. E., & Bartoe, J. D. F. 1983, ApJ, 272, 329
Chandran, B. D. G. 2010, ApJ, 720, 548
Chandran, B. D. G. 2021, JPIPh, 87, 905870304
Chew, G. F., Goldberger, M. L., & Low, F. E. 1956, RSPSA, 236, 112
Collier, M. R., Hamilton, D. C., Gloeckler, G., Bochsler, P., & Sheldon, R. B.
   1996, GeoRL, 23, 1191
Cranmer, S. R., Field, G. B., & Kohl, J. L. 1999, SSRv, 87, 149
Cranmer, S. R., & Winebarger, A. R. 2019, ARA&A, 57, 157
Czechowski, A., Ratkiewicz, R., McKenzie, J. F., & Axford, W. I. 1998, A&A,
D'Amicis, R., Perrone, D., Bruno, R., & Velli, M. 2021, JGRA, 126, e28996
David, C., Gabriel, A. H., Bely-Dubau, F., et al. 1998, A&A, 336, L90
DeForest, C. E., Hoeksema, J. T., Gurman, J. B., et al. 1997, SoPh, 175, 393
Demastus, H. L., Wagner, W. J., & Robinson, R. D. 1973, SoPh, 31, 449
Dowdy, J. F. J., Rabin, D., & Moore, R. L. 1986, SoPh, 105, 35
Drake, J. F., Agapitov, O., Swisdak, M., et al. 2021, A&A, 650, A2
Drake, J. F., Cassak, P. A., Shay, M. A., Swisdak, M., & Quataert, E. 2009,
    pJL, 700, L16
Dudok de Wit, T., Krasnoselskikh, V. V., Bale, S. D., et al. 2020, ApJS,
Finley, A. J., McManus, M. D., Matt, S. P., et al. 2021, A&A, 650, A17
Fisk, L. A., & Kasper, J. C. 2020, ApJL, 894, L4
Fox, N. J., Velli, M. C., Bale, S. D., et al. 2016, SSRv, 204, 7
```

```
Gabriel, A. H. 1976, RSPTA, 281, 339
Gabriel, A. H. 1977, in IAU Coll. 36, The Energy Balance and Hydrodynamics
   of the Solar Chromosphere and Corona (Cambridge: Cambridge Univ.
   Press), 375
Gershman, D. J., Zurbuchen, T. H., Fisk, L. A., et al. 2012, JGRA, 117,
   A00M02
Gloeckler, G., & Geiss, J. 1998, SSRv, 86, 127
Gosling, J. T., McComas, D. J., Roberts, D. A., & Skoug, R. M. 2009, ApJL,
   695, L213
Gosling, J. T., Tian, H., & Phan, T. D. 2011, ApJL, 737, L35
Hackenberg, P., Mann, G., & Marsch, E. 1999, SSRv, 87, 207
Halekas, J. S., Whittlesey, P., Larson, D. E., et al. 2020, ApJS, 246, 22
Hassler, D. M., Dammasch, I. E., Lemaire, P., et al. 1999, Sci, 283, 810
Hellinger, P., Travnicek, P., Kasper, J. C., & Lazarus, A. J. 2006, GeoRL, 33,
Hoeksema, J. T. 1984, PhD thesis, Stanford Univ.
Hollweg, J. V. 1974, JGR, 79, 1539
Horbury, T. S., Matteini, L., & Stansby, D. 2018, MNRAS, 478, 1980
Horbury, T. S., Woolley, T., Laker, R., et al. 2020, ApJS, 246, 45
Jiang, R.-L., Fang, C., & Chen, P.-F. 2012, ApJ, 751, 152
Kasper, J. C., Abiad, R., Austin, G., et al. 2016, SSRv, 204, 131
Kasper, J. C., Bale, S. D., Belcher, J. W., et al. 2019, Natur, 576, 228
Kasper, J. C., Klein, K. G., Weber, T., et al. 2017, ApJ, 849, 126
Kasper, J. C., Maruca, B. A., Stevens, M. L., & Zaslavsky, A. 2013, PhRvL,
   110, 091102
Kasper, J. C., Stevens, M. L., Korreck, K. E., et al. 2012, ApJ, 745, 162
Klein, K. G., Alterman, B. L., Stevens, M. L., Vech, D., & Kasper, J. C. 2018,
   PhRvL, 120, 205102
Kohl, J. L., Noci, G., Antonucci, E., et al. 1998, ApJL, 501, L127
Kopp, R. A., & Kuperus, M. 1968, SoPh, 4, 212
Landi, S., Hellinger, P., & Velli, M. 2005, in ESA SP-592, Solar Wind 11/
  SOHO 16, Connecting Sun and Heliosphere (Noordwijk: ESA), 785
Landi, S., Hellinger, P., & Velli, M. 2006, GeoRL, 33, L14101
Magyar, N., Utz, D., Erdélyi, R., & Nakariakov, V. M. 2021a, ApJ, 911, 75
Magyar, N., Utz, D., Erdélyi, R., & Nakariakov, V. M. 2021b, ApJ, 914, 8
Maksimovic, M., Bale, S. D., Berčič, L., et al. 2020, ApJS, 246, 62
Mallet, A., Squire, J., Chandran, B. D. G., Bowen, T., & Bale, S. D. 2021,
   arXiv:2104.08321
Marsch, E., Pilipp, W. G., Thieme, K. M., & Rosenbauer, H. 1989, JGR,
   94, 6893
Marsch, E., Rosenbauer, H., Schwenn, R., Muehlhaeuser, K. H., &
   Neubauer, F. M. 1982, JGR, 87, 35
Martinez-Sykora, J., Pontieu, B. D., Hansteen, V. H., et al. 2017, Sci,
   356, 1269
Maruca, B. A., Bale, S. D., Sorriso-Valvo, L., Kasper, J. C., & Stevens, M. L.
   2013, PhRvL, 111, 241101
Maruca, B. A., Kasper, J. C., & Gary, S. P. 2012, ApJ, 748, 137
Matteini, L., Horbury, T. S., Neugebauer, M., & Goldstein, B. E. 2014,
   GeoRL, 41, 259
McComas, D. J., Alexander, N., Angold, N., et al. 2016, SSRv, 204, 187
McComas, D. J., Barraclough, B. L., Gosling, J. T., et al. 1995, JGR, 100,
McComas, D. J., Hoogeveen, G. W., Gosling, J. T., et al. 1996, A&A, 316, 368
Meyrand, R., Squire, J., Schekochihin, A. A., & Dorland, W. 2021, JPIPh, 87,
   535870301
Neugebauer, M., Goldstein, B. E., McComas, D. J., Suess, S. T., & Balogh, A.
   1995, JGR, 100, 23389
Nolte, J. T., & Roelof, E. C. 1973, SoPh, 33, 241
```

```
Science Meeting: Beyond Discovery-Toward Understanding, ed. B. Lites
  et al. (San Francisco, CA: ASP), 196
Panasenco, O., Velli, M., D'Amicis, R., et al. 2020, ApJS, 246, 54
Panasenco, O., Velli, M., & Panasenco, A. 2019, ApJ, 873, 25
Panesar, N. K., Sterling, A. C., Moore, R. L., et al. 2018, ApJL, 868, L27
Panesar, N. K., Sterling, A. C., Moore, R. L., et al. 2019, ApJL, 887, L8
Phan, T. D., Shay, M. A., Gosling, J. T., et al. 2013, GeoRL, 40, 4475
Poletto, G. 2015, LRSP, 12, 7
Raouafi, N. E., Patsourakos, S., Pariat, E., et al. 2016, SSRv, 201, 1
Raouafi, N. E., Petrie, G. J. D., Norton, A. A., Henney, C. J., & Solanki, S. K.
  2008, ApJL, 682, L137
Raouafi, N. E., & Stenborg, G. 2014, ApJ, 787, 118
Reisenfeld, D. B., McComas, D. J., & Steinberg, J. T. 1999, GeoRL, 26, 1805
Rieutord, M., & Rincon, F. 2010, LRSP, 7, 2
Ruffolo, D., Matthaeus, W. H., Chhiber, R., et al. 2020, ApJ, 902, 94
Schatten, K. H., Wilcox, J. M., & Ness, N. F. 1969, SoPh, 6, 442
Scherrer, P. H., Schou, J., Bush, R. I., et al. 2012, SoPh, 275, 207
Schou, J., Scherrer, P. H., Bush, R. I., et al. 2012, SoPh, 275, 229
Schrijver, C. J., & De Rosa, M. L. 2003, SoPh, 212, 165
Schwadron, N. A., & McComas, D. J. 2021, ApJ, 909, 95
Shibata, K., Ishido, Y., Acton, L. W., et al. 1992, PASJ, 44, L173
Shimojo, M., Hashimoto, S., Shibata, K., et al. 1996, PASJ, 48, 123
Shimojo, M., Shibata, K., & Harvey, K. L. 1998, SoPh, 178, 379
Shimojo, M., Shibata, K., Yokoyama, T., & Hori, K. 2001, ApJ, 550, 1051
Shoda, M., Chandran, B. D. G., & Cranmer, S. R. 2021, arXiv:2101.09529
Squire, J., Chandran, B. D. G., & Meyrand, R. 2020, ApJL, 891, L2
Squire, J., Meyrand, R., Kunz, M. W., et al. 2021, arXiv:2109.03255
Stansby, D., Matteini, L., Horbury, T. S., et al. 2019a, MNRAS, 492, 39
Stansby, D., Perrone, D., Matteini, L., Horbury, T. S., & Salem, C. S. 2019b,
       A, 623, L2
Strong, K. T., Harvey, K., Hirayama, T., et al. 1992, PASJ, 44, L161
Suess, S. T., Poletto, G., Wang, A. H., Wu, S. T., & Cuseri, I. 1998, SoPh,
Takasao, S., Isobe, H., & Shibata, K. 2013, PASJ, 65, 62
Telloni, D., Sorriso-Valvo, L., Woodham, L. D., et al. 2021, ApJL, 912, L21
Teriaca, L., Poletto, G., Romoli, M., & Biesecker, D. A. 2003, ApJ, 588, 566
Thieme, K. M., Marsch, E., & Schwenn, R. 1990, AnGeo, 8, 713
Tu, C.-Y., Zhou, C., Marsch, E., et al. 2005, Sci, 308, 519
Uritsky, V. M., DeForest, C. E., Karpen, J. T., et al. 2021, ApJ, 907, 1
Vasquez, B. J., & Hollweg, J. V. 1996, JGRA, 101, 13527
Velli, M., Lionello, R., Linker, J. A., & Mikić, Z. 2011, ApJ, 736, 32
Verniero, J. L., Larson, D. E., Livi, R., et al. 2020, ApJS, 248, 5
Wang, Y. M. 1994, ApJL, 435, L153
Wang, Y.-M., & Muglach, K. 2008, SoPh, 249, 17
Wang, Y. M., & Sheeley, N. R. J. 1990, ApJ, 355, 726
Warmuth, A., & Mann, G. 2005, A&A, 435, 1123
Whittlesey, P. L., Larson, D. E., Kasper, J. C., et al. 2020, ApJS, 246, 74
Wiegelmann, T., Thalmann, J. K., & Solanki, S. K. 2014, A&ARv, 22, 78
Wilhelm, K., Abbo, L., Auchãšre, F., et al. 2011, A&ARv, 19, 35
Wilhelm, K., Abbo, L., Auchère, F., et al. 2011, A&ARv, 19, 35
Withbroe, G. L., Jaffe, D. T., Foukal, P. V., et al. 1976, ApJ, 203, 528
Woodham, L. D., Horbury, T. S., Matteini, L., et al. 2021, A&A, 650, L1
Yamauchi, Y., Suess, S. T., Steinberg, J. T., & Sakurai, T. 2004, JGRA, 109,
Yu, H. S., Jackson, B. V., Buffington, A., et al. 2014, ApJ, 784, 166
Zank, G. P., Nakanotani, M., Zhao, L. L., Adhikari, L., & Kasper, J. 2020, ApJ,
  903, 1
```

Panasenco, O., & Velli, M. 2009, in ASP Conf. Ser. 415, The Second Hinode